

Towards secondary structure prediction of longer mRNA sequences using a quantum-centric optimization scheme

Vaibhaw Kumar
IBM Quantum
 New York, USA

vaibhaw.kumar@ibm.com

Dimitris Alevras
IBM Quantum
 New York, USA

alevas@us.ibm.com

Mihir Metkar
Moderna
 Cambridge, USA

mihir.metkar@modernatx.com

Eline Welling
Fermioniq B.V.
 Amsterdam, NL

eline@fermioniq.com

Chris Cade
Fermioniq B.V.
 Amsterdam, NL

chris@fermioniq.com

Ido Niesen
Fermioniq B.V.
 Amsterdam, NL

ido@fermioniq.com

Triet Friedhoff
IBM Quantum
 New York, USA

triet.nguyen-beck@ibm.com

Jae-Eun Park
IBM Quantum
 New York, USA

parkje@us.ibm.com

Saurabh Shivpuje
Moderna
 Cambridge, USA

sshipuji@modernatx.com

Mariana LaDue
IBM Quantum
 New York, USA

mariana.ladue@ibm.com

Wade Davis
Moderna
 Cambridge, USA

wade.davis@modernatx.com

Alexey Galda
Moderna
 Cambridge, USA

alexey.galda@modernatx.com

Abstract—Accurate prediction of mRNA secondary structure is critical for understanding gene expression, translation efficiency, and advancing mRNA-based therapeutics. However, the combinatorial complexity of possible foldings, especially in long sequences, poses significant computational challenges for classical algorithms. In this work, we propose a scalable, quantum-centric optimization framework that integrates quantum sampling with classical post-processing to tackle this problem. Building on a Quadratic Unconstrained Binary Optimization (QUBO) formulation of the mRNA folding task, we develop two complementary workflows: a Conditional Value at Risk (CVaR)-based variational quantum algorithm enhanced with gauge transformations and local search, and an Instantaneous Quantum Polynomial (IQP) circuit-based scheme where training is done classically and sampling is delegated to quantum hardware. We demonstrate the effectiveness of these approaches using IBM quantum processors, solving problem instances with up to 156 qubits and circuits containing up to 950 nonlocal gates, corresponding to mRNA sequences of up to 60 nucleotides. Additionally, we validate scalability of the CVaR algorithm on a tensor network simulator, reaching up to 354 qubits in noiseless settings. These results demonstrate the growing practical capabilities of hybrid quantum-classical methods for tackling large-scale biological optimization problems.

I. INTRODUCTION

Messenger RNA (mRNA) serves as a fundamental component in gene expression, acting as the intermediary between genomic DNA and the cellular machinery responsible for protein synthesis. Its biological function is intricately linked to its secondary structure, which arises from specific base-pairing interactions and folding patterns [1]. This structural aspect is vital for understanding gene expression, regulation, translation, and the dynamics of mRNA degradation [2], and

is therefore central to both basic molecular biology and the development of mRNA-based therapeutics [3].

mRNA secondary structure prediction represents a substantial computational challenge due to the myriad potential folding configurations and associated energy considerations. The structural complexity of RNA is amplified by its six backbone torsion angles – compared to only two in proteins – increasing the range of possible structures [4]. This complexity is reflected in the Protein Data Bank, where RNA structures, particularly mRNAs, are significantly underrepresented, highlighting the need for precise computational prediction tools. Moreover, predicting structures with pseudoknots is classified as an NP-complete problem [5]. Traditional methods such as the Zuker algorithm and its derivatives, MFold and ViennaRNA, use dynamic programming to evaluate thermodynamic stability [6], [7], [8]. Enhancements such as stochastic context-free grammars in tools like Infernal [9] aid in predicting conserved structures, and the integration of machine learning in ContextFold enhances accuracy by utilizing both local and global contextual information [10]. Nevertheless, the inherent limitations of classical methods, particularly their difficulties in managing the combinatorial complexity of possible structures, have prompted a growing interest in utilizing quantum computing to address these challenges.

In a recent study [11], we evaluated the feasibility of using quantum computers to predict mRNA secondary structure, using up to 80 qubits on IBM Eagle and next-generation Heron processors. These experiments, which involved mRNA sequences of up to 42 nucleotides, represented the largest instance of such problems tackled by quantum computing to

date. However, classical algorithms [12] can process mRNA sequences with hundreds or thousands of nucleotides, but only by relying on strong approximations, such as excluding pseudoknots. Scalable alternatives are needed to model these structures more accurately. The development of quantum computing approaches offers a promising path forward. This work demonstrates substantial progress in that direction by applying quantum-centric workflows to increasingly complex instances, thereby laying a robust groundwork for further breakthroughs in the field.

There has been a significant push towards developing quantum capabilities beyond utility scale, which enables tackling increasingly complex optimization problems. However, a majority of utility-scale studies on gate-based quantum computers [13], [14], [15], [16], [17], [18], [19], [20], [21], focus on problems that align closely with the architecture of available quantum hardware. This is primarily due to the significant overhead incurred in circuit depth and gate counts when the problem structure is incompatible with the hardware layout.

Variational Quantum Algorithms (VQAs) offer a versatile approach to quantum optimization, that can be run on hardware-efficient circuits, making them applicable to a broad range of problems. Despite this adaptability, VQAs face significant challenges during the optimization phase. The task of fine-tuning circuit parameters to minimize the cost function is inherently NP-hard, often complicated by the presence of multiple local minima that can trap the optimization process [22], [23], [24], [25]. Moreover, a prevalent issue in VQAs is the emergence of barren plateaus [26], [27]. Although the challenges of multiple local minima and barren plateaus are formidable, they do not entirely preclude the potential discovery of effective parameter trajectories that may bypass these hurdles in practical settings. Further research suggests that circuits that successfully navigate these issues may, on average, be amenable to classical simulation [28]. Encouragingly, this insight provides an avenue to develop pragmatic approaches in which circuits could be trained classically, and quantum computers could then be employed primarily for sampling from these optimized circuits. Furthermore, the expressivity of the circuits significantly affects the performance of VQAs [29], underscoring the need for a balanced approach in circuit design that pays attention to the class of circuits that are difficult to classically simulate while ensuring trainability, and expressivity.

As we enter the utility era of quantum computing, the capability of quantum computing to address problems beyond the reach of conventional brute-force classical methods is rapidly becoming a reality. This advancement necessitates a careful reevaluation of how quantum and classical resources are distributed and integrated, especially as we address increasingly complex challenges beyond the utility scale. The development of a quantum-centric approach, which strategically combines quantum processors with classical compute nodes, has shown promising results in the realm of chemistry [30], [31]. This model, where the quantum processor is the focal point of

computation complemented by classical resources, provides a robust blueprint for tackling large-scale problems.

In this paper, we propose two quantum-centric approaches that orchestrate the assignment of workloads between quantum and classical compute nodes, allowing us to tackle relatively large problems. Both strategies use variational circuits. The first approach builds upon a previous work [11], where the optimal circuit parameters are found using a feedback loop between the quantum processor and classical nodes, as it is commonly done for a VQA. Following Ref. [32], parameter updates are driven by the Conditional Value at Risk (CVaR) as the objective function, based on the samples collected from the quantum processor. In this work, we additionally introduce a gauge transformation on the original Hamiltonian as a means to mitigate noise in hardware samples to improve convergence. We also implement a parameter threshold to further boost convergence during circuit executions on quantum hardware. To increase the likelihood of reaching the ground state, the mitigated samples undergo additional post-processing through a shallow local search on classical nodes. This multi-tiered approach leverages the unique strengths of both quantum and classical computing resources to ensure optimal convergence of the VQA scheme to the lowest-energy solution.

To investigate the scalability of the CVaR VQA approach, we employ tensor network methods [33], [34], [35] to simulate the quantum circuits of the VQA. By decomposing the wave function into a network of smaller tensors, each with a bond dimension that captures the amount of entanglement present in the quantum state, tensor network simulations can scale to much larger systems than is possible with state-vector simulators. States with limited entanglement can be described exactly by a tensor network state with a modest bond dimension. For highly entangled states, the bond dimension required to represent the state exactly grows exponentially with the number of qubits and must be artificially restricted – to ensure that the tensor network state fits in classical memory – at the cost of an approximation error that increases with the degree of entanglement [36], [37]. Despite this limitation, our tensor network simulations have proven crucial in validating the effectiveness of the CVaR VQA approach for tackling large problem instances, surpassing the capabilities of other types of classical simulators and of currently available quantum hardware. By exploiting the linear topology and relatively shallow depth of the VQA circuits, we successfully solve mRNA secondary structure prediction problems with up to 354 qubits. Although this validation is limited to the ideal case in which the quantum circuits are noiseless, it provides essential confirmation that the CVaR VQA scheme could remain viable on future quantum hardware, and that it can potentially scale successfully to hundreds of qubits.

In our second approach, we introduce an optimization scheme that utilizes parameterized Instantaneous Quantum Polynomial (IQP) circuits [38], [39]. We specifically select IQP circuits because the expectation values of a state prepared by such a circuit can be efficiently estimated using classical computers. However, sampling from the output distributions of

an IQP circuit is generally considered classically difficult [40], [41], [42]. It is worth noting that the presence of noise can complicate these hardness assumptions [43]. We outline a strategy, also described in Refs. [44], [45], wherein the training of a parameterized IQP circuit occurs entirely on a classical computer, using expectation values as the objective metric. The quantum computer's role is then limited to sampling bitstrings from the circuit containing optimal parameters. To enhance the quality of these samples, we employ an error mitigation technique that utilizes classically computed single-qubit expectation values to adjust for noise present in the quantum hardware outputs. Similar to our first method, we also apply a lightweight local search algorithm to further enhance the probability of reaching the ground state. This dual-stage optimization harnesses the strengths of both classical and quantum computing, providing a robust framework to improve convergence.

Our results provide a promising path towards solving longer mRNA sequences using a quantum-centric approach. Using this workflow, we have successfully examined mRNA sequences of length up to 60 nucleotides corresponding to problem sizes that require up to 156 qubits. The experiments involve quantum circuits with up to 950 gates and circuit depths up to 112. This scale of quantum computation not only highlights the growing capabilities of quantum hardware but also underscores the potential for significant advancements in understanding complex biological structures through quantum-assisted methodologies.

The paper is organized as follows. In Section II, we provide a concise description of the Quadratic Unconstrained Binary Optimization (QUBO) formulation of the mRNA secondary structure prediction problem. Section III is dedicated to detailing the methodologies employed in this research, as well as discussing the results obtained from the examination of several mRNA sequences. Lastly, Section IV offers a summary of our findings and provides an outlook on future directions of this research.

II. QUBO FORMALISM

In this Section, we provide an overview of the QUBO formulation used to model the mRNA secondary structure prediction problem.

Each position in an RNA sequence, indexed by $i = 1, \dots, n$, is occupied by one of the nucleotide bases: U, A, C , or G . Base pairing between two positions i and j is deemed valid if the bases form one of the following pairs: $\{(AU), (UA), (CG), (GC), (GU), (UG)\}$. Further, the decision variable represents a quartet which is defined as two consecutive base pairs, often referred to as stacked pairs which is represented by the tuple $(i, j, i+1, j-1)$, where (i, j) and $(i+1, j-1)$ indicate the positions of the two consecutive base pairs.

Following the framework established in Ref. [46], we define the quartet (stacked pair) variable as::

$$x(i, j, i+1, j-1) = \begin{cases} 1 & \text{if stacking occurs between base pairs } (i, j) \text{ and } (i+1, j-1) \\ 0 & \text{otherwise.} \end{cases}$$

Note that these variables are established exclusively for valid base pairs. The model incorporates constraints based on specific rules to ensure valid RNA structures. One crucial rule is that each base can be paired with only one other base, effectively preventing multiple pairings for any single base within the sequence. Additionally, two quartets cannot be selected simultaneously if their base pairs cross each other, which is formalized in the constraint:

$$x(i, j, i+1, j-1) + x(k, \ell, k+1, \ell-1) \leq 1. \quad (1)$$

This type of constraint is also observed in the independent set problem [47]. Defining q_i as the variable for the i^{th} quartet and denoting Q as the set of all valid quartets, QC as the set of crossing quartet pairs, $QS(q_i)$ as the set of quartets that can be stacked with q_i , and QUA as the set of stacked quartets ending in a (UA) pair, we express the corresponding QUBO problem as follows:

$$\begin{aligned} \min \sum_{q_i \in Q} e_{q_i} q_i + r \sum_{q_i \in Q} \sum_{q_j \in QS(q_i)} q_i q_j \\ + p \sum_{q_i \in Q} \sum_{q_j \in QUA} q_i (1 - q_j) + t \sum_{q_i, q_j \in QC} q_i q_j. \end{aligned} \quad (2)$$

The QUBO formulation in Eq. (2) includes terms that capture the energy contributions of individual quartets within the RNA structure. Each quartet variable q_i is assigned a free energy e_{q_i} derived from empirical thermodynamic data, as described in Ref. [48], and contributes to the objective function through the term $e_{q_i} q_i$. Stability contributions from consecutive quartets, which are known to enhance RNA structural stability, are explicitly rewarded in the model. This is captured by the reward factor r and is incorporated into the objective function as $r \sum_{q_i \in Q} \sum_{q_j \in QS(q_i)} q_i q_j$. In addition, the model imposes penalties to discourage structurally unfavorable configurations. For example, sequences ending in a less stable (UA) pair are penalized using a factor p , implemented through the term $p \sum_{q_i \in Q} \sum_{q_j \in QUA} q_i (1 - q_j)$, following the energetics described in Ref. [48]. The constraints that prevent the formation of crossing quartets are modeled with a penalty factor t as $t \sum_{q_i, q_j \in QC} q_i q_j$. For computational implementation, we utilize the Qiskit [49] framework that facilitates the conversion of such problems into QUBO format and assists in calculating penalties for the constraints. The transformation from QUBO's Boolean variables to spin variables, which are then represented using Pauli Z matrices, is essential for formulating the Hamiltonian $H_p = \sum_i Z_i + \sum_i \sum_{j(i)} J_{ij} Z_i Z_{j(i)}$, where $j(i)$ denotes all variables that share a quadratic term with variable x_i in the original QUBO.

The QUBO problems in this work, derived from the secondary structure prediction of mRNA sequences, typically exhibit high edge densities in their corresponding problem graphs, ranging from approximately 0.7 to 0.85. This indicates

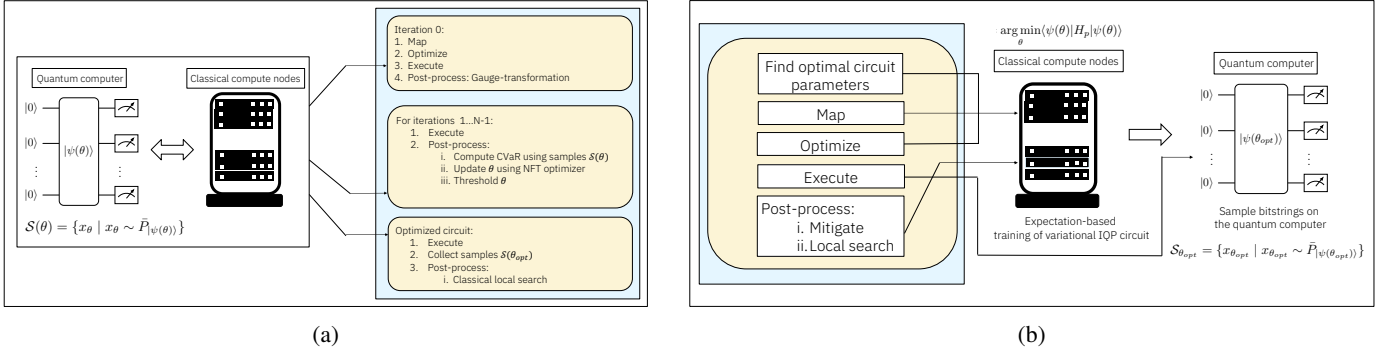


Fig. 1: a) Schematic for the quantum-centric architecture for sampling-based quantum optimization using CVaR. The training of the variational circuit is carried out by collecting hardware samples S_θ characterized by the noisy distribution $\bar{P}_{|\psi(\theta)\rangle}$ and processing them on the classical compute nodes. b) Schematic of the approach based on the IQP circuit. Training of the variational circuit is conducted only on the classical compute nodes. The quantum processor is used for sampling from the optimized circuit.

a high level of connectivity between variables, reflecting the complex interactions within mRNA structures.

III. METHODS AND RESULTS

A. Sampling-based quantum optimization using CVaR

In Fig. 1a, we present the quantum-centric workflow for sampling-based quantum optimization. This methodology uses a variational circuit characterized by a two-local ansatz illustrated in Fig. 2a to prepare the parameterized state $|\psi(\theta)\rangle$. The search for the ground state is executed collaboratively between quantum processors and classical nodes, which are closely integrated within a quantum-centric compute cluster to maximize computational efficiency.

In the first iteration, both the mapping and optimization steps are performed on the classical node. The two-qubit CZ gates of the two-layer ($p = 2$) ansatz are arranged in a “pairwise” pattern: in the first layer, qubit i is entangled with qubit $(i + 1)$, for all even values of i , and in the second layer, qubit i is entangled with qubit $(i + 1)$ for all odd values of i . These entangling gates are mapped onto the native heavy-hex topology of the IBM quantum hardware. In the optimization step, the circuit is transpiled using Qiskit Primitive V2 transpiler with the optimization level set to 3. Dynamical decoupling is employed for error suppression using the default ‘XX’ sequence. The resulting transpiled circuit is then executed on the quantum processor using the Qiskit’s sampling primitive, with $N_{\text{shots}} = 2^{15}$ measurement samples collected.

1) *Gauge-transformed Hamiltonian*: In the pre-fault-tolerance era of quantum computing, mitigating hardware noise is crucial for achieving reliable and accurate results. To address this challenge, we adopt gauge transformations, a method previously explored for reducing the impact of noise in quantum computations [50], [51]. Notably, this approach has also been employed in an adaptive strategy known as Noise Directed Adaptive Remapping (NDAR) [20], which dynamically applies gauge transformations at each iteration

under the assumption that quantum hardware is biased towards an all-zero quantum state.

Bit-flip gauge transformations, in this context, can be interpreted as applying permutations to the diagonal problem Hamiltonian, $H_p \rightarrow \bigotimes_{i=1}^n X^{m_i} H_p \bigotimes_{i=1}^n X^{m_i}$ with $m_i \in \{0, 1\}$, indicating which qubits undergo the transformation, as described in Ref. [20]. This operation preserves the eigenvalues of H_p while inducing bit-flips in the corresponding eigenstates of the Hamiltonian. For example, in a three-qubit system with initial eigenstates $E_0 : 000, E_1 : 011, \dots$, applying a gauge transformation to the middle qubit would modify the eigenstates to $E_0 : 010, E_1 : 001, \dots$.

The suitability of gauge transformations in our context is further highlighted by the structural similarities between our QUBO problem constraints, Eq. (1), and those found in the graph-theoretic independent set problem, as discussed in Section II. This problem involves selecting a subset of nodes such that no two connected by an edge are included simultaneously. Such a task becomes particularly challenging in dense graphs. For instance, in a complete graph where each node connects to every other node, an all-zero bitstring becomes the only viable solution. Given the high density typical of our QUBO problem graphs, the feasible and optimal solutions are likely to be bitstrings with relatively low Hamming weights. However, if noisy hardware samples generally display Hamming weights higher than those expected from a noiseless circuit, the optimization process can be significantly slowed down. By applying the gauge transformation, we align the characteristics of noisy hardware samples with the relevant eigenstates of the transformed problem Hamiltonian, thus facilitating more rapid and effective convergence during optimization.

Careful initialization of the circuit parameters allows us to compare noisy hardware samples against samples expected from a noiseless circuit without requiring additional calibration circuits. At iteration 0, we set the rotation angle θ_i to $\frac{\pi}{4}$ for a small randomly selected fraction f of qubits in the first layer, as shown in Fig. 2a, while setting other rotation angles to zero,

and maintaining the CZ gates unchanged. The application of the gate $e^{-i\frac{\pi}{4}Y}$, which can induce bit flips by creating an equal superposition of $|0\rangle$ and $|1\rangle$, is limited to a few qubits, rest of the qubits stay as $|0\rangle$. As a result, this initialization circuit aims to generate an initial state that predominantly supports bitstrings with relatively low Hamming weight under noiseless settings.

We observe that noisy hardware samples typically exhibit a higher average Hamming weight compared to the ideal, noiseless samples. For instance, a 127-qubit initialization circuit on `ibm_kyiv` results in an average Hamming weight of 17, with a standard deviation of 3 when averaged over 2^{15} samples, when a Hamming weight of 9 is expected from the noiseless circuit. This discrepancy is likely due to gate and readout errors, causing some qubits that should ideally be in the $|0\rangle$ state to be erroneously read as $|1\rangle$. To address this issue, we compute the noisy single-qubit expectation value $\langle Z_i \rangle_{\text{noisy}}$ for all qubits. We identify qubits whose noiseless expectation $\langle Z_i \rangle_{\text{noiseless}}$ should be +1 (indicative of the qubit's noiseless state as $|0\rangle$) but display $\langle Z_i \rangle_{\text{noisy}} < -p_{th}$, i.e. less than a certain cut-off p_{th} , indicating such qubits are predominantly in the noisy $|1\rangle$ state in the hardware samples. We set the cut-off to $p_{th} = 0.8$. A gauge transformation is then applied to these specific qubits in the Hamiltonian. Given the assumption that the optimal bitstring contains only a few bits as ones (owing to low Hamming weight), it is highly probable that this gauge transformation will flip the bit values from $0 \rightarrow 1$ at the identified qubit locations in the original optimal bitstring. Consequently, this procedure constructs a new Hamiltonian, calibrated to reflect the hardware sample's Hamming weight distribution more accurately. This transformation is applied only once at iteration 0.

Following the initialization at iteration 0, as illustrated in Fig. 1a, we proceed with further iterations up to the total N_{iter} . These subsequent iterations involve repeated cycles between the quantum hardware and classical nodes. After each execution of the circuit, the samples are used on the classical nodes to compute the CVaR value [32]. CVaR is the mean of the lowest α -tail of the energy distribution of the samples, which quantifies the expected value of the best outcomes. This metric has been identified as more robust against noise when used as an objective function in quantum computations [13]. CVaR-based parameter updates are carried out using the classical NFT optimizer [52] named after the authors Nakanishi, Fujii, and Todo, which has demonstrated enhanced convergence properties in a recent study [53]. For CVaR calculations, we select $\alpha = 0.2$ similar to the value used in Ref. [11].

2) *Parameter threshold:* To improve convergence on quantum hardware, we implement a circuit parameter thresholding scheme that has been used in recent quantum optimization studies [19], [17]. In this scheme, any circuit parameters where $|\theta_i| < \theta_{th}$ are set to zero. For our experiments, we established, after few quick runs, that applying the threshold $\theta_{th} = 0.06$ substantially improves convergence.

The total number of iterations, N_{iter} , is chosen to ensure

convergence of the CVaR-based objective to a stable minimum. Since each iteration in the NFT optimization scheme updates only a single parameter, N_{iter} must be large enough to complete at least two full passes over all circuit parameters. The parameters are updated in a randomized order within each epoch.

3) *Post-processing:* After N_{iter} iterations, the circuit characterized by θ_{opt} is expected to generate sample bitstrings close to the ground state. To enhance the likelihood of identifying the optimal solution, we implement a post-processing step using a computationally efficient classical local-search scheme. This approach has been recognized in recent studies as an effective method to refine raw hardware samples [16], [54].

The local search algorithm, detailed in Algorithm 1, systematically attempts to improve the bitstrings by applying a single bit flip per step. Each of the n bits undergoes one trial flip, executed in a random order determined by a uniformly distributed sequence. This flip is facilitated by the function $\text{Flip}(\mathbf{x}, j)$, targeting the j^{th} bit of bitstring \mathbf{x} . If a flip reduces the energy, the new bitstring is accepted; otherwise, the change is rejected, and the process continues with the next bit flip attempted on the accepted bitstring at the bit index next in order in the random sequence (see Algorithm 1).

Ideally, if all trial flips are accepted, this process could alter the original bitstring by a Hamming distance of n . As a result, the decrease in the objective value that can be introduced by the local search is always $\leq \Delta = 2(\sum_i h_i + \sum_{(i,j) \in G} J_{ij})$. Hence, for the local search to find the optimal state with high probability, it is important that the energy difference between the objective value of the mitigated sample E_s and the optimal solution E_g should not exceed Δ , underscoring the need for mitigated sample energies E_s to be sufficiently close to energy E_g of the optimal solution. While various advanced local search methods like Tabu search [55] exist in the classical literature and can effectively solve problems independently, they generally struggle with problems beyond a certain size. In such cases, the goal of our quantum-centric approach is to leverage the quantum processor to handle the computationally intensive tasks, bringing the system closer to the optimal solution. Subsequently, a classical local solver can be employed to fine-tune and determine the precise optimal solution.

Algorithm 1 Local Search Algorithm

Input: : A bit string $\mathbf{x} \in \mathcal{S}(\theta_{opt})$ of length n ; objective function obj

Output: : A bit string with improved objective

```

for  $j$  in  $\text{Permute}(\mathbf{x})$  do
     $\mathbf{x}^* = \text{Flip}(\mathbf{x}, j)$ 
    if  $obj(\mathbf{x}^*) < obj(\mathbf{x})$  then
         $\mathbf{x} \leftarrow \mathbf{x}^*$ 
    end if
end for

```

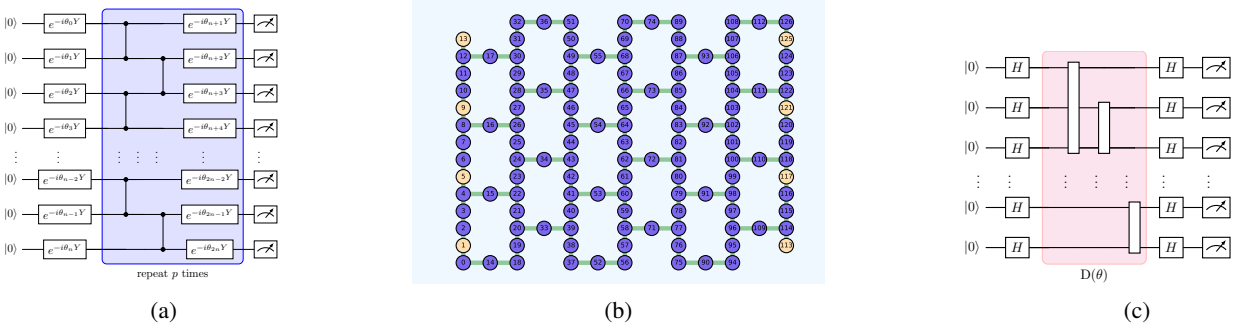


Fig. 2: a) The two-local ansatz with p repetitions of characterized by parameterized Pauli-Y single-qubit rotations and two-qubit CZ gates b) IQP-circuit's heavy-hex-based tubular arrangement of two qubit $e^{-i\theta ZZ}$ rotation gates on the `ibm_kyiv` heavy-hex layout with edges between yellow-colored qubits along with all the edges on the heavy-hex graph, shown in green c) parameterized IQP-circuit where $D(\theta)$ represents the diagonal unitary of the form $e^{-i \otimes_j \theta_j Z_j^{m_j}}$ where $m_j \in \{0, 1\}$.

4) *Hardware results:* We examine 133 and 150 qubit problems originating from mRNA sequences of length 60 and 48, respectively. The 133 qubit problem, originally sized at 256 qubits, was effectively reduced using the strategy outlined in Appendix A. The circuits for these utility scale experiments, comprising 133 and 150 qubits, included 700 and 939 non-local gates respectively on the Heron r2 processor `ibm_marrakesh`.

Fig. 5 displays the energy distributions from the final iteration alongside those refined via a local-search-based post-processing technique. The comparison reveals that while the raw hardware samples are nearly optimal, local search further sharpens the distribution, enhancing the proximity to the ground state. As discussed in Ref. [11], these runs require extensive computational efforts. Specifically, for 200 iterations, the process involves approximately $3 \times N_{\text{shots}} \times N_{\text{iter}}$ circuit executions, totaling about $600 \times 2^{15} \sim 10^7$ executions demonstrating robustness of IBM Qiskit Runtime primitive driven quantum-centric workflow in handling such large-scale experiments.

The ability to simulate quantum circuits using classical methods is a crucial area that requires thorough exploration to advance toward achieving quantum advantage. Tensor network-based methods [36] are a leading choice for the simulation of quantum circuits. Using these tools, we can gain enhanced insight into the simulation overheads associated with various circuit layouts and sizes, as well as assess the effectiveness of these heuristic strategies in an ideal noise-free setting. In the following, we detail a tensor network-based approach specifically designed for the two-local ansatz employed in this work.

B. Tensor network simulations

In this Section, we describe the tensor network method developed to simulate the CVaR VQA algorithm, which accurately mirrors its implementation on (noiseless) quantum hardware.

1) *Tensor network method:* We utilize a tensor network state to represent the quantum state prepared by the parame-

terized circuit. After each parameter update, we draw samples from this tensor network state to compute the CVaR, which then informs subsequent parameter adjustments.

The parameterized quantum circuit in our study features a one-dimensional connectivity pattern, making it suitable for representation using a Matrix Product State (MPS) [56], [57], [58]. Given the circuit's shallow depth, characterized by only a few layers of gates, an MPS with an adequately large bond dimension can exactly capture the state generated by the circuit.

The initial state (including the first layer of single-qubit parameterized gates) is a product state and therefore representable by an MPS with a bond dimension of $\chi = 1$. The rest of the circuit is composed of layers of CZ gates followed by single-qubit rotations. A single CZ-gate is a rank-2 tensor, as can be seen from the following decomposition $\text{CZ} = |0\rangle\langle 0| \otimes I + |1\rangle\langle 1| \otimes Z$. Therefore, a CZ gate can be decomposed into a two-site Matrix Product Operator (MPO) with a bond dimension of 2. Using the above decomposition, a layer of nearest-neighbor CZ gates on n qubits can be represented by a single n -qubit MPO also of bond dimension 2. The parameterized single-qubit gates applied after the CZ gates can be contracted into the n -qubit CZ MPO without increasing its MPO bond dimension. Consequently, each layer of the parameterized circuit can be exactly represented by a single n -qubit MPO with an MPO bond dimension of $D = 2$, see Figure 3.

An MPS description of the state prepared by the parameterized circuit is obtained as follows. Starting with the initial product state represented as an MPS of bond dimension $\chi = 1$, each layer of the quantum circuit is directly contracted into the MPS. Since each layer is represented by an MPO of bond dimension 2, contracting it exactly into the MPS doubles the MPS bond dimension χ . When a circuit parameter is changed, the MPS can be efficiently updated by only modifying the single local tensor affected by the change.

After each parameter update, the CVaR is computed by efficiently sampling from the MPS through parallelized sample drawing [59]. The sampling process utilizes the ability

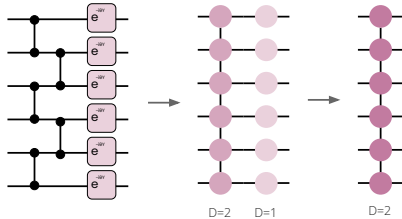


Fig. 3: Depiction of a single layer of the parameterized quantum circuit, consisting of an entangling layer of CZ gates followed by a layer of parameterized single-qubit gates. Together, the gates form an n -qubit MPO with a bond dimension of 2.

to efficiently compute single-site reduced density matrices (RDMs) by combining the MPS with its complex conjugate and contracting across all but one of the physical sites. Sampling then proceeds qubit-by-qubit, where for each qubit the RDM is computed and a sample basis state is drawn from the resulting probability distribution. After drawing a sample, the physical index is fixed and the process moves to the next site. This method ensures that all samples are independent and suitable for CVaR computation.

All of the steps above have a runtime that scales (at most) linearly in system size, making the above method of exact circuit contraction well suited for investigating how the algorithm presented in Section III-A scales with increasing qubit number. For example, for a 560-qubit problem instance with two ansatz layers, the total time it took to update a parameter and corresponding local MPS tensor, draw 2^{15} samples, and compute the CVaR was less than a second in total (and less than 0.1 second for the < 100-qubit VQA instances) on a single NVIDIA GH200 GPU.

Increasing the number of layers in the circuit rapidly makes exact contraction computationally intractable. Indeed, a circuit with p layers requires an MPS of bond dimension $\chi = 2^p$ in order to absorb the circuit exactly, and the time it takes to update a local tensor, which only depends on the number of layers, scales as $O(4^p)$. Additionally, the time it takes to draw a sample scales as $O(n\chi^3)$ for the pre-processing plus $O(n\chi^2)$ per sample, resulting in a total runtime of $O(n(8^p + n_s 4^p))$ for n_s samples. In order to simulate deeper circuits, approximate contraction routines (at the cost of an approximation error), such as those used in IBM's Qiskit MPS simulator, or those used in Fermioniq's Ava and in Refs. [36], [37], [60] are required. However, these approximate contraction routines are significantly more time consuming, resulting in simulation times reaching minutes (or even hours for particularly challenging circuits) per circuit simulation, making them much less suitable for VQA simulations that easily require thousands of circuit simulations in total.

2) *Tensor network results:* Using the method described in the previous Section, we explore how the quantum algorithm behaves for larger system sizes. In particular, we simulate the same algorithm discussed in Section III-A (using two ansatz

layers) for VQA instances of up to 406 qubits to investigate its performance with increasing system size. Table I displays how often (out of 100 runs) the algorithm succeeds in finding the optimal solution (hit rate), both with and without classical post-processing. From the table we observe that (i) post-processing increases the hit rate, and (ii) the hit rate decreases rapidly with increasing system size.

Qubits	Without post-processing		With post-processing	
	Hits	γ	Hits	γ
40	40	-	85	-
80	9	-	60	-
114	2	-	12	-
164	2	-	6	-
212	0	0.7%	1	-
264	0	4.5%	1	-
354	0	21.4%	0	10.5%
406	0	30.3%	0	20.4%

TABLE I: Number of times the optimal solution was found out of 100 runs for increasing number of qubits with and without post processing. For systems where the optimal solution was not found, the table shows the relative error to the optimal solution.

When the optimal solution is not found, the relative error, given by $\gamma = \frac{|F(\theta_f)_{\text{low}} - F_0|}{|F_0|} \times 100\%$, signifies how close the obtained solution is to the optimal solution, where $F(\theta_f)_{\text{low}}$ represents the lowest value of the objective function (over all samples) obtained at any time during the simulation, and F_0 denotes the value of the objective function of the optimal solution found by CPLEX. From Table I we observe that as the system size increases, so does the relative error, indicating that the algorithm has increasing difficulty finding optimal solutions as the number of qubits grows.

These observations raise two key questions: (i) whether running additional optimization epochs improves convergence, and (ii) whether the current ansatz—with only two layers of entangling gates—has sufficient expressivity to produce high-quality solutions as the number of qubits increases. Our simulations indicate that simply adding many more epochs does not lead to significant improvements in the average relative error of the best solution, albeit that the first few epochs added do slightly reduce the error. However, performance can also be modestly improved by resuming optimization from the *best* parameter configuration encountered during an epoch, rather than from the *last* one obtained throughout an epoch. Applying this strategy, we successfully solve the 354-qubit problem instance, correctly finding the known optimal solution.

Increasing the number of layers in the circuit while keeping the rest of the algorithm unchanged (i.e., running optimization for two epochs) also fails to improve performance, likely due to the optimizer struggling with the larger parameter space. We find that a layer-wise optimization strategy, in which layers are added incrementally and only the parameters of the newly added layer are updated while previous layers are held fixed, does improve convergence. This approach reduces the

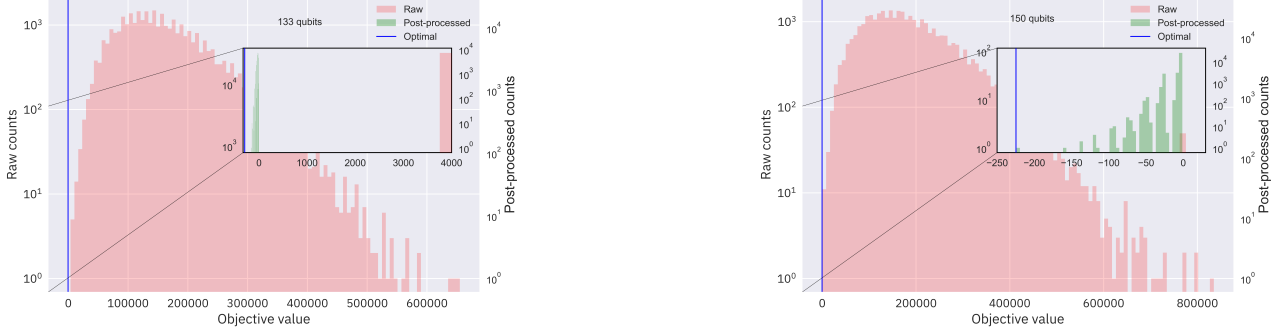


Fig. 4: The converged unnormalized raw objective value distributions from the hardware experiments on `ibm_marrakesh` for the a) 133 and b) 150 qubit experiments. Inset shows the post-processed distributions using the local search scheme. Blue solid lines indicate the optimal objective values of -295.4 and -224.65 for the 133 and 150 qubit problems, respectively (found by CPLEX). In both the cases, we are able to find the optimal solution after post-processing.

effective number of parameters optimized at each step, easing the burden on the optimizer.

It is possible that the observed improvements from adding more layers stem primarily from the increased number of optimization steps, rather than from greater circuit expressivity. Indeed, further experiments show that much of this extra performance could be obtained by just running the algorithm to convergence with a fixed number of layers (when continuing from the best parameter configuration encountered during each epoch). However, these experiments do still suggest that additional layers might yield some improvement.

Overall, we cannot draw any strong conclusions regarding possible solutions to the decreasing algorithm performance with increasing qubit number. Using tensor network simulations, we found several promising directions, but these will need to be studied more rigorously in future work if we are to meaningfully improve the algorithm performance on larger problem instances.

Finally, we remark that the effects of hardware noise on the performance of the algorithm have not been considered in our simulations. It is likely that noise worsens the algorithm performance, but it is not clear exactly how and whether this effect is greater for larger numbers of qubits. The tensor network methods that we have described in this section are capable of simulating the effects of noise, and we leave it to future work to investigate the performance of the algorithm using noisy simulations.

C. IQP circuit-based optimization

The sampling-based scheme described in Section III-A requires multiple circuit executions over several iterations on the hardware. The IQP-circuit-based optimization we propose here attempts to alleviate this problem. IQP circuits are a special class of quantum circuits characterized by commuting gates. The parameterized IQP circuit, as shown in Fig. 2c, can be represented by a unitary $U(\theta) = H^{\otimes n}D(\theta)H^{\otimes n}$, where $D(\theta) = \prod_j e^{-i\theta_j \otimes_{i=1}^n Z_i^{m_i}}$ is a diagonal operator (in the computational basis) and bitstring $m \in \{0, 1\}^n$ specifies

the gate locations. H and Z denote the Hadamard and Pauli-Z gates, respectively.

The output distribution of an IQP circuit is generally considered classically intractable to sample from, making it a potential candidate for demonstrating quantum advantage [40], [41], [42]. Interestingly, while sampling from these circuits is challenging, expectation values can be efficiently computed classically up to $\text{poly}(n^{-1})$ error [61]. This unique characteristic of the IQP circuit is leveraged in our approach to optimize the balance between quantum and classical computational capabilities, aiming to enhance the overall efficiency and feasibility of computational tasks.

The optimization of the parameterized IQP circuit is achieved through a variational approach, where the expectation value $E_\theta = \langle 0|U^\dagger(\theta)H_PU(\theta)|0\rangle$ serves as the objective function. Given that the expectation values of observables related to our problem Hamiltonian can be efficiently computed on a classical computer, we determine the optimal circuit parameters entirely via classical computational means. Subsequently, the presumably classically challenging task of sampling is performed on quantum hardware using the circuit configured with these optimal parameters. In situations where E_θ does not converge sufficiently on the classical computer, one can also envision an alternate scheme where the search for better circuit parameters can be carried out using a CVaR-based sampling (see Section III-A) on the quantum computer. The ability to calculate the ideal single-qubit expectation values efficiently on a classical computer also facilitates error mitigation. This dual approach harnesses the strengths of both classical and quantum computing to improve accuracy and reliability in quantum experiments.

In Fig. 1b, we show the workflow for the quantum-centric IQP-circuit-based scheme. The task of finding the optimal parameters that minimize the expectation value $\theta_{opt} = \arg \min_\theta \langle \psi(\theta) | H_p | \psi(\theta) \rangle$ is carried out entirely on the classical compute nodes. Parameterized ansatz uses the diagonal operator characterized by single qubit $e^{-i\theta Z}$ and two-qubit

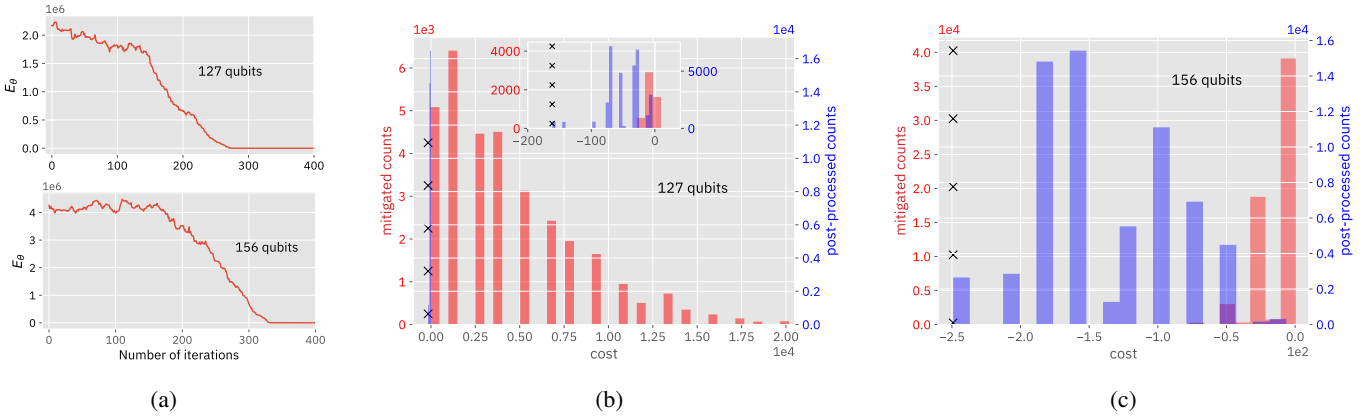


Fig. 5: a) Convergence plots for the expectation value E_θ obtained by training the variational circuit on classical nodes for the 127 and 156 qubit problem, b) and c) indicate the mitigated and post-processed (using local solver) unnormalized objective value distributions using red and blue bars, respectively. The plots correspond to hardware runs for 127 qubit and 156 qubit on `ibm_kyiv` and `ibm_marrakesh`, respectively. The black ‘x’ denotes the optimal objective values of -161.5 and -249.1 for the 127 and 150 qubit problems respectively, as determined by CPLEX.

$e^{-i\theta ZZ}$ rotations. The two qubit gates are arranged over a tubular heavy-hex layout as shown in Fig. 2b. We perform N_{iter} iterations of the variational scheme. Circuit parameters are initialized using random values drawn from a uniform distribution over the interval $[0, 2\pi]$. The expectation calculation for a quantum state prepared using an IQP circuit consists of computing averages over bit strings generated randomly from a uniform distribution (see Appendix B). We use a recently developed JAX-based library to compute the expectation values [44] using 2^{15} sample bitstrings. The circuit parameters are updated at each iteration using the NFT optimizer [52]. The value of N_{iter} is set to a sufficiently large value where the expectation values reach a plateau.

After map and optimize steps on classical nodes as outlined in Section III-A, the circuit parameterized by θ_{opt} is executed on the quantum processor. The raw samples thus obtained are then subjected to post-processing on classical nodes. Initially, this involves using an IQP-circuit-based approach for error mitigation. Given that single-qubit observables from IQP circuits can also be computed efficiently, we use the classically computed noiseless single-qubit expectation values $\langle Z_i \rangle$ to correct the samples. For qubits where the absolute expectation values $|\langle Z_i \rangle|$ exceed a predefined positive threshold $\langle Z_i \rangle_{th}$, which we set at 0.99, the qubit is highly likely to be in a state of $|0\rangle$ or $|1\rangle$. Such qubits are accordingly set to 0 or 1 in the raw samples, while those not meeting this threshold are retained as is. In the subsequent post-processing phase, the mitigated samples undergo further refinement through a local search technique as described in Section III-A3.

1) *Hardware results:* In order to examine the performance of the proposed scheme we performed experiments on 127 and 156 qubit problems corresponding to mRNA sequence lengths of 45 and 60 nucleotides, respectively. We use the reduction scheme (Appendix A) to create the 156 qubit problem from an original 256 qubit problem. The 127 and 156

qubit experiments were conducted on IBM’s Eagle processor `ibm_kyiv` and Heron r2 processor `ibm_marrakesh`, respectively. These circuits are characterized by total circuit depths up to 112 and consists of approximately 450 non-local gates. We use dynamical decoupling with the default “XX” sequence for error suppression. In Fig. 5a, we show the evolution of the expectation values E_θ during the variational scheme carried out on the classical nodes. As observed in the plots, E_θ gradually reaches a plateau after approximately 320 iterations. In Figs. 5b and 5c, we present the mitigated and post-processed unnormalized objective value distributions for the 127 and 156 qubit experiments. It is clear from the plot that the mitigated hardware distribution is already relatively close to the ground state. This allows the local search scheme to find the ground state with a relatively high probability.

In contrast with the line-based connectivity utilized for the two-local ansatz (refer to Section III-A), we employ a tubular heavy-hex structure here. Deviation from the one-dimensional circuit layout serves as the first step to discover circuits with better convergence properties that are at the same time also hard to classically simulate for sampling tasks.

Our results provide evidence that parameterized IQP circuit-based optimization can serve as a promising tool to investigate optimization problems.

IV. CONCLUSIONS AND OUTLOOK

In this study, we have introduced a quantum-centric optimization workflow that strategically utilizes both quantum and classical computing resources to effectively tackle the problem of predicting the secondary structure of longer mRNA sequences. Our approach, which incorporates a novel IQP-based sampling scheme, not only facilitates good convergence but also takes a step further towards delegating classically difficult tasks to the quantum computer. Additionally, the custom error mitigation strategies we developed significantly enhance the

quality of the noisy samples obtained from quantum hardware, motivating further exploration of such techniques in sampling-based approaches and other problem domains.

Tensor network simulations of the CVaR VQA played a supportive role in this study, contributing to the validation of the quantum algorithm performance. By enabling simulations of larger quantum systems, tensor networks have complemented the capabilities of current quantum hardware, especially in scenarios involving an increased number of qubits. This support has helped to evaluate the effectiveness of these approaches and identify areas for potential methodological improvements.

Our work indicates that problem-agnostic circuits based on the hardware topology are of practical relevance. However, the theoretical foundations of such fixed-architecture circuits remain less explored [62]. Future research will aim to strategically design connectivity layouts that enhance performance.

Our implementation demonstrates that the variational scheme can reach sufficient convergence, leading to circuits that can create samples in the vicinity of the ground state. However, due to the heuristic nature of such schemes, it is difficult to provide performance guarantees as the problems scale. This underscores the need for more extensive testing with larger problem instances. Additionally, we plan to explore non-variational schemes such as Bias Field Counterdiabatic scheme [19], [17] and quantum enhanced MCMC [63], which rely on problem-inspired circuits. These methods necessitate the development of advanced techniques for embedding these problem-specific circuits into the existing quantum hardware topology, aiming to minimize the overhead associated with gate counts.

ACKNOWLEDGMENTS

The authors thank Yashrajsinh Jadeja and Haining Lin for their contributions to the prediction of classical RNA secondary structures. Fermioniq was supported by the Dutch National Growth Fund (NGF), as part of the Quantum Delta NL Programme.

APPENDIX

A. Reduction Scheme

We describe a problem reduction scheme we have developed to reduce the number of problem variables. Let the mRNA secondary structure prediction problem, as described in Section II, has its general QUBO form, $Q = \sum_i h_i x_i + \sum_i \sum_{j(i)} J_{ij} x_i x_j$.

The proposed reduced scheme is possible because of the following two properties of Q .

- 1) The coefficients of the linear terms are much smaller in magnitude than the coefficients of the quadratic terms i.e. $|h_i| \ll |J_{ij}|$
- 2) Q contains a subset κ of variables k whose quadratic coefficients $J_{kj} \geq 0$ for $\forall j(k)$.

Due to the properties above, for any assignment of variables in κ , their contributions to Q will always be ≥ 0 . As a result, one can only focus on variables $\notin \kappa$ and formulate a reduced QUBO, $Q_{\text{red}} = \sum_{i \notin \kappa} (h_i x_i + \sum_{j(i) \notin \kappa} J_{ij} x_i x_j)$ containing

$n - |\kappa|$ variables where n is the original problem size. After we have found the optimal solution to Q_{red} , the task at hand is to find the assignment of variables $\in \kappa$ that gives the lowest cost. This in turn requires finding the optimal solution to

$$Q_{\kappa} = \sum_{i \in \kappa} (h_i x_i + \sum_{j(i) \in \kappa} J_{ij} x_i x_j + \sum_{j(i) \notin \kappa} J_{ij} x_i x_j) \quad (3)$$

As we have already found the optimal assignments of the variables $\notin \kappa$ by solving Q_{red} , this information can be used to find the optimal assignment of the variables $\in \kappa$. It is clear from Eq. (3), if $x_j = 1$ in $\sum_{j(i) \notin \kappa} J_{ij} x_i x_j$, then x_i must be assigned a value of 0 because setting them to 1 is guaranteed to increase the objective Q_{κ} . Only the subset of variables κ whose quadratic contribution $\sum_{i \in \kappa} \sum_{j(i) \notin \kappa} J_{ij} x_i x_j$ is equal to zero (owing to x_j s equal to zero) and the coefficient of the linear term $h_i < 0$ can lower the value of Q_{κ} . In order to find their optimal assignment, one needs to solve another QUBO, with the objective function as $Q_{\kappa} = \sum_{i \in \kappa} (h_i x_i + \sum_{j(i) \in \kappa} J_{ij} x_i x_j)$. In our problems, the number of variables $\in \kappa$ is relatively small and can usually be solved by exact enumeration.

B. Computing expectations from parameterized IQP circuit

If the IQP circuit is denoted by the unitary $U(\theta) = H^{\otimes n} \prod_j e^{i\theta_j \otimes_{i=1}^n Z_i^{m_i}} H^{\otimes n}$, where $m \in \{0, 1\}^n$, the expectation E_{θ} corresponding to the observable $\bigotimes_{k=1}^n Z_k^{p_k}$, where $p_k \in \{0, 1\}^n$ can be written as

$$\begin{aligned} & \langle + |^{\otimes n} \prod_j e^{i\theta_j \otimes_{i=1}^n Z_i^{m_i}} H^{\otimes n} \bigotimes_{k=1}^n Z_k^{p_k} H^{\otimes n} \prod_j e^{-i\theta_j \otimes_{i=1}^n Z_i^{m_i}} | + \rangle^{\otimes n} \\ &= \frac{1}{2^n} \sum_{x \in \{0, 1\}^n} e^{i \sum_j \theta_j (-1)^{m \cdot x}} \langle x | \bigotimes_{k=1}^n X_k^{p_k} \sum_{y \in \{0, 1\}^n} e^{-i \sum_j \theta_j (-1)^{m \cdot y}} | y \rangle \\ &= \frac{1}{2^n} \sum_{x \in \{0, 1\}^n} e^{i \sum_j \theta_j (-1)^{m \cdot x}} \langle x | \sum_{y \in \{0, 1\}^n} e^{-i \sum_j \theta_j (-1)^{m \cdot y}} | y \oplus p \rangle \\ &= \frac{1}{2^n} \sum_{y \in \{0, 1\}^n} e^{i \sum_j \theta_j (-1)^{\sum_k m_k (y_k \oplus p_k - y_k)}} \end{aligned} \quad (4)$$

Note (\cdot) denotes bitwise dotproduct and \oplus denotes addition modulo 2. As expectation is guaranteed to be real valued, we can write

$$E_{\theta} = \frac{1}{2^n} \sum_{y \in \{0, 1\}^n} \cos \left[\sum_j \theta_j (-1)^{\sum_k m_k (y_k \oplus p_k - y_k)} \right], \quad (5)$$

which can be calculated by computing the empirical mean $\mathbb{E}_{y \sim U} \cos \left[\sum_j \theta_j (-1)^{\sum_k m_k (y_k \oplus p_k - y_k)} \right]$ over the sample bitstrings y drawn from a uniform distribution U .

REFERENCES

- [1] Q. Vicens and J. S. Kieft, "Thoughts on how to think (and talk) about RNA structure," *Proceedings of the National Academy of Sciences*, vol. 119, no. 17, p. e212677119, 2022.

[2] M. Metkar, C. S. Pepin, and M. J. Moore, “Tailor made: the art of therapeutic mRNA design,” *Nature Reviews Drug Discovery*, vol. 23, no. 1, pp. 67–83, 2024.

[3] S. Qin, X. Tang, Y. Chen, K. Chen, N. Fan, W. Xiao, Q. Zheng, G. Li, Y. Teng, M. Wu *et al.*, “mRNA-based therapeutics: powerful and versatile tools to combat diseases,” *Signal Transduction and Targeted Therapy*, vol. 7, no. 1, p. 166, 2022.

[4] J. Zhang, M. Lang, Y. Zhou, and Y. Zhang, “Predicting rna structures and functions by artificial intelligence,” *Trends in Genetics*, 2024.

[5] R. B. Lyngsø and C. N. Pedersen, “RNA pseudoknot prediction in energy-based models,” *Journal of Computational Biology*, vol. 7, no. 3-4, pp. 409–427, 2000.

[6] M. Zuker, “Computer prediction of RNA structure,” in *Methods in enzymology*. Elsevier, 1989, vol. 180, pp. 262–288.

[7] M. Zuker, “Mfold web server for nucleic acid folding and hybridization prediction,” *Nucleic Acids Research*, vol. 31, no. 13, pp. 3406–3415, 2003.

[8] P. Schuster, P. F. Stadler, and A. Renner, “RNA structures and folding: from conventional to new issues in structure predictions,” *Current Opinion in Structural Biology*, vol. 7, no. 2, pp. 229–235, 1997.

[9] E. P. Nawrocki and S. R. Eddy, “Infernal 1.1: 100-fold faster RNA homology searches,” *Bioinformatics*, vol. 29, no. 22, pp. 2933–2935, 2013.

[10] S. Zakov, Y. Goldberg, M. Elhadad, and M. Ziv-Ukelson, “Rich parameterization improves RNA structure prediction,” *Journal of Computational Biology*, vol. 18, no. 11, pp. 1525–1542, 2011.

[11] D. Alevras, M. Metkar, T. Yamamoto, V. Kumar, T. Friedhoff, J.-E. Park, M. Takeori, M. LaDue, W. Davis, and A. Galda, “mrna secondary structure prediction using utility-scale quantum computers,” in *2024 IEEE International Conference on Quantum Computing and Engineering (QCE)*, vol. 1. IEEE, 2024, pp. 488–499.

[12] S. Yang, N. T. Pham, Z. Li, J. Y. Baik, J. Lee, T. Zhai, W. Yu, B. Hou, T. Shang, W. He *et al.*, “Advances in rna secondary structure prediction and rna modifications: Methods, data, and applications,” *arXiv preprint arXiv:2501.04056*, 2025.

[13] S. V. Barron, D. J. Egger, E. Pelofske, A. Bärtschi, S. Eidenbenz, M. Lehmkuhler, and S. Woerner, “Provably bounds for noise-free expectation values computed from noisy samples,” *Nature Computational Science*, pp. 1–11, 2024.

[14] A. Miessen, D. J. Egger, I. Tavernelli, and G. Mazzola, “Benchmarking digital quantum simulations and optimization above hundreds of qubits using quantum critical dynamics,” *arXiv preprint arXiv:2404.08053*, 2024.

[15] S. H. Sack and D. J. Egger, “Large-scale quantum approximate optimization on nonplanar graphs with machine learning noise mitigation,” *Physical Review Research*, vol. 6, no. 1, p. 013223, 2024.

[16] N. Sachdeva, G. S. Hartnett, S. Maity, S. Marsh, Y. Wang, A. Winick, R. Dougherty, D. Canuto, Y. Q. Chong, M. Hush *et al.*, “Quantum optimization using a 127-qubit gate-model ibm quantum computer can outperform quantum annealers for nontrivial binary optimization problems,” *arXiv preprint arXiv:2406.01743*, 2024.

[17] S. V. Romero, A.-M. Visuri, A. G. Cadavid, E. Solano, and N. N. Hegade, “Bias-field digitized counterdiabatic quantum algorithm for higher-order binary optimization,” *arXiv preprint arXiv:2409.04477*, 2024.

[18] Á. Nodar, I. De León, D. Arias, E. Mamedaliev, M. E. Molina, M. Martín-Cordero, S. Hernández-Santana, P. Serrano, M. Arranz, O. Mentxaka *et al.*, “Scaling the variational quantum eigensolver for dynamic portfolio optimization,” *arXiv preprint arXiv:2412.19150*, 2024.

[19] A. G. Cadavid, A. Dalal, A. Simen, E. Solano, and N. N. Hegade, “Bias-field digitized counterdiabatic quantum optimization,” *arXiv preprint arXiv:2405.13898*, 2024.

[20] F. B. Maciejewski, J. Biamonte, S. Hadfield, and D. Venturelli, “Improving quantum approximate optimization by noise-directed adaptive remapping,” *arXiv preprint arXiv:2404.01412*, 2024.

[21] L. Leclerc, C. Dalyac, P. Bendotti, R. Griset, J. Mikael, and L. Henriet, “Implementing transferable annealing protocols for combinatorial optimization on neutral-atom quantum processors: A case study on smart charging of electric vehicles,” *Physical Review A*, vol. 111, no. 3, p. 032611, 2025.

[22] L. Bittel and M. Kliesch, “Training variational quantum algorithms is np-hard,” *Physical review letters*, vol. 127, no. 12, p. 120502, 2021.

[23] E. Fontana, M. Cerezo, A. Arrasmith, I. Rungger, and P. J. Coles, “Non-trivial symmetries in quantum landscapes and their resilience to quantum noise,” *Quantum*, vol. 6, p. 804, 2022.

[24] E. R. Anschuetz and B. T. Kiani, “Quantum variational algorithms are swamped with traps,” *Nature Communications*, vol. 13, no. 1, p. 7760, 2022.

[25] M. Larocca, P. Czarnik, K. Sharma, G. Muraleedharan, P. J. Coles, and M. Cerezo, “Diagnosing barren plateaus with tools from quantum optimal control,” *Quantum*, vol. 6, p. 824, 2022.

[26] J. R. McClean, S. Boixo, V. N. Smelyanskiy, R. Babbush, and H. Neven, “Barren plateaus in quantum neural network training landscapes,” *Nature communications*, vol. 9, no. 1, p. 4812, 2018.

[27] M. Larocca, S. Thanaislp, S. Wang, K. Sharma, J. Biamonte, P. J. Coles, L. Cincio, J. R. McClean, Z. Holmes, and M. Cerezo, “A review of barren plateaus in variational quantum computing,” *arXiv preprint arXiv:2405.00781*, 2024.

[28] M. Cerezo, M. Larocca, D. García-Martín, N. Diaz, P. Braccia, E. Fontana, M. S. Rudolph, P. Bermejo, A. Ijaz, S. Thanaislp *et al.*, “Does provable absence of barren plateaus imply classical simulability,” *Or, why we need to rethink variational quantum computing*, 2023.

[29] A. Tikku and I. H. Kim, “Circuit depth versus energy in topologically ordered systems,” *arXiv preprint arXiv:2210.06796*, 2022.

[30] J. Robledo-Moreno, M. Motta, H. Haas, A. Javadi-Abhari, P. Jurcevic, W. Kirby, S. Martiel, K. Sharma, S. Sharma, T. Shirakawa *et al.*, “Chemistry beyond exact solutions on a quantum-centric supercomputer,” *arXiv preprint arXiv:2405.05068*, 2024.

[31] D. Kaliakin, A. Shajan, J. R. Moreno, Z. Li, A. Mitra, M. Motta, C. Johnson, A. A. Saki, S. Das, I. Sitzdikov *et al.*, “Accurate quantum-centric simulations of supramolecular interactions,” *arXiv preprint arXiv:2410.09209*, 2024.

[32] P. K. Barkoutsos, G. Nannicini, A. Robert, I. Tavernelli, and S. Woerner, “Improving variational quantum optimization using cvar,” *Quantum*, vol. 4, p. 256, 2020.

[33] U. Schollwöck, “The density-matrix renormalization group in the age of matrix product states,” *Annals of physics*, vol. 326, no. 1, pp. 96–192, 2011.

[34] D. Lykov, R. Schutski, A. Galda, V. Vinokur, and Y. Alexeev, “Tensor network quantum simulator with step-dependent parallelization,” in *2022 IEEE International Conference on Quantum Computing and Engineering (QCE)*. IEEE, 2022, pp. 582–593.

[35] R. Orús, “A practical introduction to tensor networks: Matrix product states and projected entangled pair states,” *Annals of physics*, vol. 349, pp. 117–158, 2014.

[36] Y. Zhou, E. M. Stoudenmire, and X. Waintal, “What limits the simulation of quantum computers?” *Physical Review X*, vol. 10, no. 4, p. 041038, 2020.

[37] T. Ayral, T. Louvet, Y. Zhou, C. Lambert, E. M. Stoudenmire, and X. Waintal, “Density-matrix renormalization group algorithm for simulating quantum circuits with a finite fidelity,” *PRX Quantum*, vol. 4, no. 2, p. 020304, 2023.

[38] S. P. Jordan, “Permutational quantum computing,” *arXiv preprint arXiv:0906.2508*, 2009.

[39] D. J. Shepherd, “Quantum complexity: restrictions on algorithms and architectures,” *arXiv preprint arXiv:1005.1425*, 2010.

[40] M. J. Bremner, R. Jozsa, and D. J. Shepherd, “Classical simulation of commuting quantum computations implies collapse of the polynomial hierarchy,” *Proceedings of the Royal Society A: Mathematical, Physical and Engineering Sciences*, vol. 467, no. 2126, pp. 459–472, 2011.

[41] M. J. Bremner, A. Montanaro, and D. J. Shepherd, “Average-case complexity versus approximate simulation of commuting quantum computations,” *Physical review letters*, vol. 117, no. 8, p. 080501, 2016.

[42] S. C. Marshall, S. Aaronson, and V. Dunjko, “Improved separation between quantum and classical computers for sampling and functional tasks,” *arXiv preprint arXiv:2410.20935*, 2024.

[43] J. Rajakumar, J. D. Watson, and Y.-K. Liu, *Polynomial-Time Classical Simulation of Noisy IQP Circuits with Constant Depth*. Society for Industrial and Applied Mathematics, Jan. 2025, p. 1037–1056. ISBN 9781611978322. [Online]. Available: <http://dx.doi.org/10.1137/1.9781611978322.30>

[44] E. Recio-Armengol and J. Bowles, “Iqopt: Fast optimization of instantaneous quantum polynomial circuits in jax,” *arXiv preprint arXiv:2501.04776*, 2025.

[45] E. Recio-Armengol, S. Ahmed, and J. Bowles, “Train on classical, deploy on quantum: scaling generative quantum machine learning to a thousand qubits,” *arXiv preprint arXiv:2503.02934*, 2025.

[46] D. Gusfield, *Integer Linear Programming in Computational and Systems Biology: An Entry-Level Text and Course*. Cambridge University Press, 2019.

[47] F. Glover, G. Kochenberger, and Y. Du, “A tutorial on formulating and using qubo models,” *arXiv preprint arXiv:1811.11538*, 2018.

[48] D. H. Turner and D. H. Mathews, “NNDDB: the nearest neighbor parameter database for predicting stability of nucleic acid secondary structure,” *Nucleic Acids Research*, vol. 38, no. suppl_1, p. D280– D282, 2009.

[49] Qiskit contributors, “Qiskit: An open-source framework for quantum computing,” 2023.

[50] E. Pelofske, G. Hahn, and H. Djidjev, “Optimizing the spin reversal transform on the d-wave 2000q,” in *2019 IEEE International Conference on Rebooting Computing (ICRC)*. IEEE, 2019, pp. 1–8.

[51] A. Barbosa, E. Pelofske, G. Hahn, and H. N. Djidjev, “Optimizing embedding-related quantum annealing parameters for reducing hardware bias,” in *Parallel Architectures, Algorithms and Programming: 11th International Symposium, PAAP 2020, Shenzhen, China, December 28–30, 2020, Proceedings 11*. Springer, 2021, pp. 162–173.

[52] K. M. Nakanishi, K. Fujii, and S. Todo, “Sequential minimal optimization for quantum-classical hybrid algorithms,” *Phys. Rev. Res.*, vol. 2, p. 043158, Oct 2020. doi: 10.1103/PhysRevResearch.2.043158

[53] M. Oliv, A. Matic, T. Messerer, and J. M. Lorenz, “Evaluating the impact of noise on the performance of the variational quantum eigensolver,” *arXiv preprint arXiv:2209.12803*, 2022.

[54] M. Sciorilli, L. Borges, T. L. Patti, D. García-Martín, G. Camilo, A. Anandkumar, and L. Aolita, “Towards large-scale quantum optimization solvers with few qubits,” *Nature Communications*, vol. 16, no. 1, p. 476, 2025.

[55] F. Glover and M. Laguna, *Tabu search*. Springer, 1998.

[56] M. Fannes, B. Nachtergael, and R. F. Werner, “Finitely correlated states on quantum spin chains,” *Communications in mathematical physics*, vol. 144, pp. 443–490, 1992.

[57] S. Östlund and S. Rommer, “Thermodynamic limit of density matrix renormalization,” *Physical review letters*, vol. 75, no. 19, p. 3537, 1995.

[58] G. Vidal, “Efficient classical simulation of slightly entangled quantum computations,” *Physical review letters*, vol. 91, no. 14, p. 147902, 2003.

[59] J. Wegemann, M. Folkertsma, and C. Cade, “Guidable local hamiltonian problems with implications to heuristic ansatz state preparation and the quantum pcp conjecture,” in *19th Conference on the Theory of Quantum Computation, Communication and Cryptography*, 2024.

[60] A. P. Thompson, A. Soeteman, C. Cade, and I. Niesen, “Non-zero noise extrapolation: accurately simulating noisy quantum circuits with tensor networks,” *arXiv preprint arXiv:2501.13237*, 2025.

[61] M. Nest, “Simulating quantum computers with probabilistic methods,” *arXiv preprint arXiv:0911.1624*, 2009.

[62] E. Farhi, J. Goldstone, S. Gutmann, and H. Neven, “Quantum algorithms for fixed qubit architectures,” *arXiv preprint arXiv:1703.06199*, 2017.

[63] D. Layden, G. Mazzola, R. V. Mishmash, M. Motta, P. Wocjan, J.-S. Kim, and S. Sheldon, “Quantum-enhanced markov chain monte carlo,” *Nature*, vol. 619, no. 7969, pp. 282–287, 2023.